

## An assessment method of rail corrugation based on wheel–rail vertical force and its application for rail grinding

Niu, Liubin; Yang, Fei; Deng, Xiangyun; Zhang, Pan; Jing, Guoqing; Qiang, Weile; Guo, Yunlong

**DOI**

[10.1007/s13349-023-00700-w](https://doi.org/10.1007/s13349-023-00700-w)

**Publication date**

2023

**Document Version**

Final published version

**Published in**

Journal of Civil Structural Health Monitoring

**Citation (APA)**

Niu, L., Yang, F., Deng, X., Zhang, P., Jing, G., Qiang, W., & Guo, Y. (2023). An assessment method of rail corrugation based on wheel–rail vertical force and its application for rail grinding. *Journal of Civil Structural Health Monitoring*, 13(4-5), 1131-1150. <https://doi.org/10.1007/s13349-023-00700-w>

**Important note**

To cite this publication, please use the final published version (if applicable).  
Please check the document version above.

**Copyright**

Other than for strictly personal use, it is not permitted to download, forward or distribute the text or part of it, without the consent of the author(s) and/or copyright holder(s), unless the work is under an open content license such as Creative Commons.

**Takedown policy**

Please contact us and provide details if you believe this document breaches copyrights.  
We will remove access to the work immediately and investigate your claim.



# An assessment method of rail corrugation based on wheel–rail vertical force and its application for rail grinding

Liubin Niu<sup>1</sup> · Fei Yang<sup>1</sup> · Xiangyun Deng<sup>2</sup> · Pan Zhang<sup>3</sup> · Guoqing Jing<sup>4</sup> · Weile Qiang<sup>1</sup> · Yunlong Guo<sup>3</sup> 

Received: 25 July 2022 / Accepted: 9 April 2023  
© The Author(s) 2023

## Abstract

In practice, the assessment and treatment of rail corrugation are quantitatively based on the corrugation depth. Wheel–rail vertical forces (WRVF), as a direct reflection of wheel–rail interaction, can give expression to the corrugation depth and thus serve as a key parameter for assessing the corrugation. In this paper, we propose an evaluation method for rail corrugation based on the WRVF. First, a 3D wheel–rail dynamic finite element (FE) model was developed with typical parameters of CRTS II slab track and CRH3 vehicle for high-speed railways in China. The accuracy of the model was then validated with the measured WRVF data in the field. Second, using the validated model, the time–frequency domain distribution of WRVF (vehicle speed: 300 km/h) was obtained with consideration of the corrugation wavelength in the range of 40–180 mm. The non-linear least squares method and rational equation were used to fit the function between the large value of WRVF and the corrugation depth value under the conditions of different corrugation wavelengths. Next, effects of the Pinned–Pinned resonance frequency and vibration mode on the fitted parameters were analysed, by which an indicator for corrugation treatment (grinding) was proposed. Finally, the indicator was applied in the monitoring of rail corrugation for high-speed railway lines in the field. The results show that the misjudgement rate of rail grinding decisions (using the proposed indicator) is low with the accuracy at 92.5%. The proposed method can provide a basis for the rail corrugation evaluation and grinding decisions-making.

**Keywords** High speed rail · FE modelling · Wheel–rail vertical forces · Corrugation assessment · Grinding decision

## 1 Introduction

Rail corrugation the wavy roughness at the railhead surface along the longitudinal direction. It occurs after train operation for some time. As shown in Fig. 1, healthy rail has flat railhead surface and even width of a rail running surface, whereas corrugated rail has wavy railhead surface

and uneven width of the running surface. Rail corrugation is accompanied by different kinds of rail running surface. For example, the seriously worn positions form the corrugation troughs, where the rail running surface is wider; the lightly worn positions form corrugation peaks, where the rail running surface is slightly narrower. The rail running surface under normal condition, mild corrugation and severe corrugation can be observed in Fig. 1a–c. The presence of rail corrugation can cause various types of damages in the vehicle-track system, for example the separation of fasteners from the rubber mats (Fig. 1d) and the breaking of fasteners (Fig. 1e, f).

Nowadays, as railways are operated at much higher speeds, rail corrugation causes high-frequency vibrations of wheels and rails, leading to increasingly prominent problems, such as noises, fatigue, damage to components of vehicle (e.g. out-of-round wheels) and track and permanent deformation of track sub-structures (e.g. ballast, subgrade) [1–3]. In addition, the rail corrugation consumes additional power traction energy and increases track maintenance costs.

✉ Xiangyun Deng  
xydeng@seu.edu.cn

✉ Yunlong Guo  
yunlong.guo@tudelft.nl

<sup>1</sup> Infrastructure Inspection Research Institute, China Academy of Railway Sciences Co., Ltd., Beijing 100081, China

<sup>2</sup> School of Civil Engineering, Southeast University, Nanjing 210096, China

<sup>3</sup> Faculty of Civil Engineering and Geosciences, Delft University of Technology, 2628CN Delft, The Netherlands

<sup>4</sup> School of Civil Engineering, Beijing Jiaotong University, Beijing 100044, China

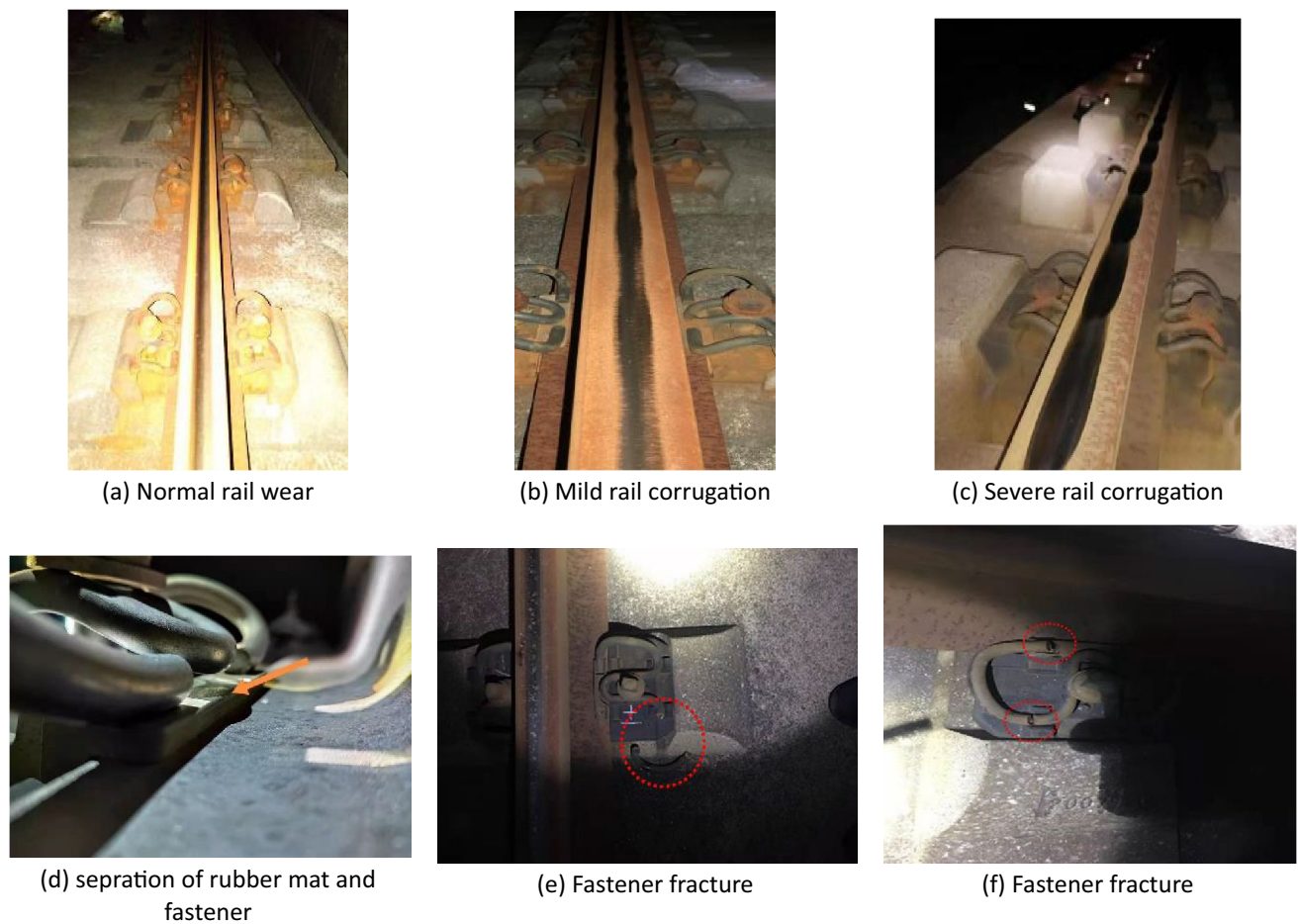


**Fig.1** Three types of rail corrugations and rail running surfaces

If rail corrugation is not treated/remedied in time, the deterioration of the wheel–rail interaction reduces the vehicle running quality, and in some extreme cases it can even lead to destructive damages to the track structure and thus endanger the running safety of vehicles [4, 5].

Although rail corrugation has been reported over one century worldwide, no universal theory for its cause has been developed. Some studies were able to explain the occurrence and development of specific types of rail corrugation. Some treatment measures were accordingly proposed for these types of rail corrugation. For example, in the review works in [6–8], rail corrugation were divided into six categories based on the wavelength (frequency) and causes. They included Pinned–Pinned resonance (roaring rails), rutting, heavy haul, light rail, other P2 resonance and track form-specific. Accordingly, causes, characteristics, and treatments were discussed for these types of corrugation.

The works in [11–14] reviewed the field investigations and the distribution of corrugation characteristics in the wavelength range 25–80 mm found in different countries. Assumptions were further made for the causes

of corrugation. Additionally, the patterns of corrugation growth were analysed using numerical and experimental methods. Finally, the effects of maintenance and mitigation measures were discussed on slowing down the corrugation growth, such as increasing the hardness of rail materials, friction modifier, rail vibration absorbers.

Due to the complexity of the corrugation formation and growth, however, so far there is not a commonly accepted and effective rail corrugation treatment method. Rail grinding can reduce the rapid corrugation growth, which has become a widely used means to control rail corrugation [15–17]. Accurate identification of corrugation status is necessary for performing rail grinding. The rail surface roughness level [18] (or corrugation depth value [19]) is normally used to identify the severity of corrugation. Then decision is made on whether to grind or not.

Traditionally, corrugation depth was manually measured using corrugation CAT. Compared to the manual measurement, new inspection technologies can efficiently and precisely identify the corrugation. These technologies have been embedded on the comprehensive inspection

trains developed by China Academy of Railway Sciences-CARS [20] for track health monitoring. The technologies on the inspection train and corresponding methods include:

- Laser camera technology [21] to measure the rail profile,
- Ultrasonic and eddy current detection [22] to test current changes,
- Vehicle acceleration [23] to reflect the rail surface unevenness,
- Axle box accelerations [24, 25] to perform spectral analysis and time–frequency representations,
- Wheelset with four strain gauges [26–28] to directly measure the wheel–rail contact force, etc.

Among these methods, wheelset with four strain gauges can be used to measure WRVF, which is able to directly reflect the wheel–rail interaction during vehicle operation. Particularly, the WRVF in high-frequency domain is an important parameter for assessing corrugation and corrugation growth prediction [26, 27]. Thus, the measurement of WRVF is widely used in corrugation monitoring.

Some existing researches have studied the correlation between rail surface roughness and WRVF in the frequency domain, for example, the work in [28]. In this work, the Rayleigh-Timoshenko beam finite elements were used to simulate the rail to study the power spectral density of WRVF considering viscoelastic models of rail pads and ballast/subgrade. The rail surface roughness was measured at the locations in the field, where the peak WRVF was greater than 160 kN. The effectiveness of peak wheel–rail force to identify the corrugation with the wavelength in the range of 40–80 mm was verified.

In [29], an expression was proposed for the function between the effective value of the WRVF and the rail surface roughness. Specifically, to characterise the wheel–rail responses excited by corrugation, the effective value of the WRVF in the frequency range from 500 to 1350 Hz was chosen as the index. Afterwards, in [30], using the above function, the WRVF monitoring threshold under the train speeds of 150–200 km/h was calculated. The monitoring threshold was used to provide the basis for corrugation identification and performing rail grinding.

These studies have proved that the WRVF can be used to identify and assess rail corrugation level. Most of these studies focussed on the correlations between the peak or effective value of the WRVF and the corrugation depth under fixed wavelength conditions. Limited studies considered the influence of corrugation wavelength on the correlations. However, corrugation is quasi-periodic (wave shape), characterised by certain wavelengths and depths, as shown in Fig. 1. The corrugation wavelength is a sensitive factor for wheel–rail interaction [31, 32], which is related

to the frequency and magnitude of the WRVF. In addition, the WRVF in different frequency domains have different effects on the track [33]. Therefore, studying the variation of WRVF along with different corrugation wavelengths can help to deepen the understanding of the corrugation-caused consequences. Therefore, it is great important to develop an accurate and reasonable corrugation level assessment technique based on WRVF for rail maintenance guidance.

In this paper, an explicit FE method was used to develop a three-dimensional wheel–rail dynamic model. The model is validated by the measured WRVF in the field. Afterwards, the characteristics of WRVF under the conditions of different corrugations were analysed (train speed: 300 km/h). The change rate of rail surface irregularity was proposed to characterise the corrugation. The non-linear least squares method and irrational equations were used to fit the correlation between the WRVF and the change rate of rail surface irregularity. Based on the correlation, the variation curve of the fitting coefficient with the corrugation wavelength was given. In addition, the influence of the wheelset and rail natural modes on the fitting coefficient was analysed. On this basis, the method of assessing the corrugation depth based on the WRVF was proposed, and the field measurement verified the feasibility of the assessing method. The research results can provide scientific support for rail corrugation level assessment and grinding decision in high-speed railway lines.

The structure of this paper is as follows.

- First, the 3D wheel–rail FE model is introduced, as well as the means of modelling corrugation. Then, the model validation is described.
- Second, using the validated model, simulations of different conditions are performed considering different corrugation wavelength effects on WRVF. Based on that, the indicator for rail grinding is introduced and validated.
- Finally, the conclusions are given.

## 2 Wheel–rail dynamic FE model

This section describes the wheel–rail dynamic model in detail. Three parts, i.e. modelling of the wheel–rail dynamic, corrugation simulation and model validation are included.

### 2.1 Modelling of wheel–rail dynamics

To study the wheel–rail vertical vibration characteristics in straight line with rail corrugation, a wheel–rail dynamic model is constructed with the FE code ABAQUS. The model includes a single rail, rail track structure and a half wheelset, as shown in Fig. 2. The car body and



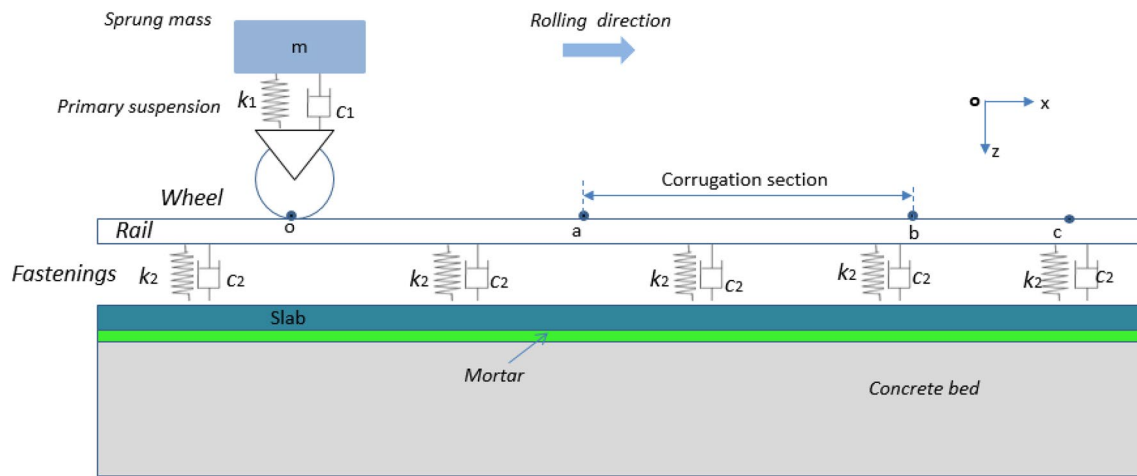


Fig. 2 Illustration of wheel–rail dynamic FE model basic principle

components above the suspension system were simplified to a mass block. The vehicle suspension system was simplified to vertical and lateral spring and damping units, which connect the mass block and wheelset.

The purpose of the model simplification is to produce most reliable results, while reducing the computation cost at the same time. The excitation frequency of the wheel–rail interaction in the corrugated rail section is calculated using Eq. 1. In this equation,  $f$  is the excitation frequency (unit Hz);  $v$  is the vehicle speed (mm/s);  $\lambda$  is the corrugation wavelength (mm). For 40–180 mm wavelengths and vehicle speeds over 300 km/h, the frequency of corrugation excitation is greater than 462.9 Hz. As stated in [34], the WRVF in this frequency band are less related to the motion of the vehicle components, such as vehicle's suspension, bogie and car body.

$$f = \frac{v}{\lambda} \quad (1)$$

Point O is set as the starting position of the simulation and Point c is the end position of the simulation. Sections oa and bc are set to be normal rails, while Section ab in the middle is set to be the rail with corrugation. The running time of the wheelset passes through the corrugation section is short, so the other movements of wheelset (e.g. wheel rotation) were not considered in the simulation.

The track length in the model is 46.66 m. It contains 72 sleepers with the spacing of 650 mm between adjacent sleepers. The overall view of the model is shown in Fig. 3. The wheel and rail were modelled using the realistic geometry of the 380B trailer (train type) wheel and CN60 rail profile. CN60 is normal rail type used in China high-speed railway. A bilinear elastic–plastic material model was used for the wheel and rail. The vehicle suspension

system is simulated by a spring and damper between the mass block M and the wheelset. The lateral movements of the wheelset and mass block were constrained. A 1:40 rail inclination was considered.

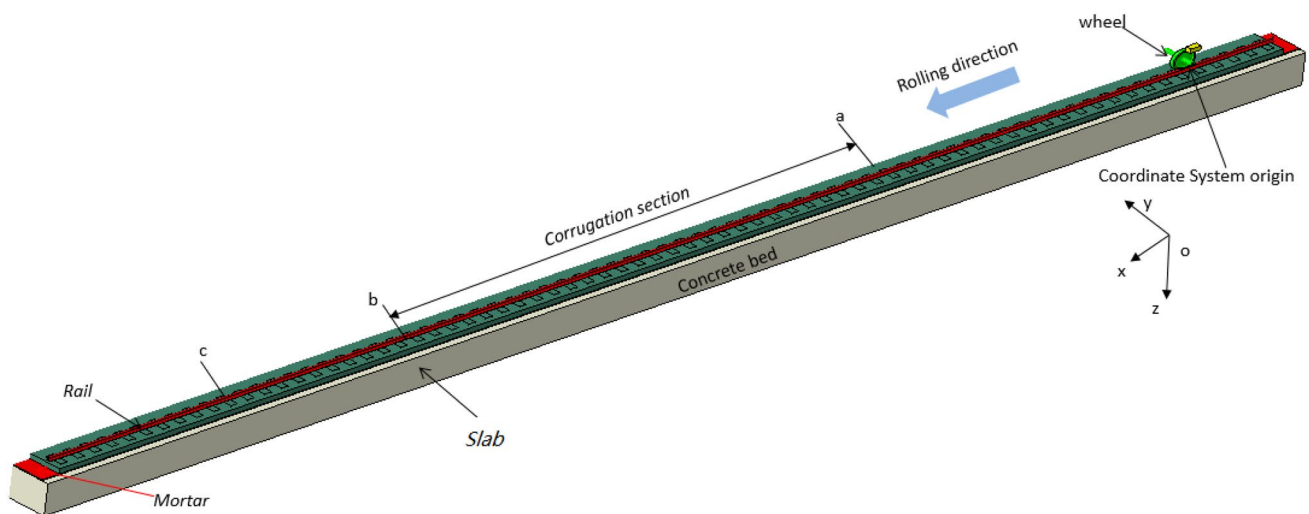
The lateral and longitudinal degrees of freedom was constrained to the contact position between the rail and the fastener. Each of fastener–rail interactions was simulated by spring and damper group, as shown in Fig. 3b. Each spring group consists of  $5 \times 11$  springs.

To reduce the calculation time of the model, non-uniform mesh was employed. Specifically, smaller mesh sizes were applied to the wheel–rail contact, and larger mesh sizes were applied to the rail bottoms, axles, track slab, CA mortar layers and other components away from the wheel–rail contact. The wheel–rail contact surface was meshed with hexahedral cells, and the minimum size was set to be  $2 \text{ mm} \times 2 \text{ mm} \times 2 \text{ mm}$ , as shown in Fig. 3b.

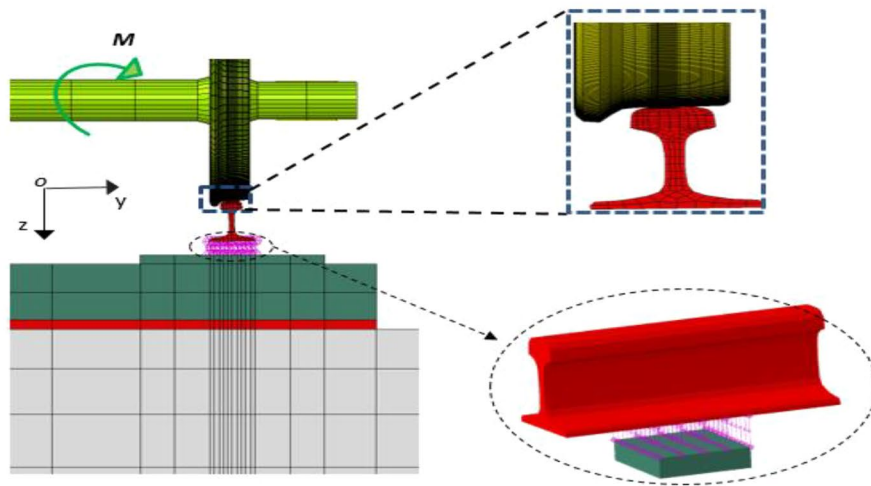
The model was solved using explicit integration scheme with central difference method. The solutions of the motion and the contact force in time domain can be obtained. In the solution, the wheel–rail contact conditions (forces, displacements, etc.) at the end of each timestep are calculated from the displacement, velocity and acceleration at the beginning of that timestep [35]. The maximum timestep is determined by the highest intrinsic frequency of the modelled components (rail, wheel, track slab, etc.) and meets the following equation.

$$\Delta t \leq \frac{2}{\omega_{\max}} \left( \sqrt{1 + \zeta^2} - \zeta \right) = \min \left( \frac{L_c}{c_d} \right) \quad (2)$$

$$c_d = \sqrt{\frac{E}{\rho}} \quad (3)$$



(a) Model overall view



(b) Details about meshes in model

**Fig. 3** Solid units and meshes for wheel–rail dynamic FE model

where  $\zeta$  is the critical damping ratio of the wheel–rail system;  $L_e$  is the length of the model meshes;  $c_d$  is the wave speed determined by the properties of the model material;  $E$  is the modulus of elasticity of the wheel and rail materials;  $\rho$  is the density of the wheel and rail materials.

The hard "face-to-face" contact algorithm was used to deal with wheel–rail normal contact forces. The friction coefficient set to 0.3 according to the study [36]. To reduce the computation cost, an implicit algorithm was first used to calculate the static equilibrium state of the model under gravity. The result was afterwards used as the initial boundary condition for the explicit calculation.

A traction torque  $M$  is applied to the wheels to reduce the effect of wheel–rail friction on the running speed, which is to ensure wheelset running at uniform speed. The value of the traction torque  $M$  is obtained from Eq. 4 [37].

$$M - F_x R = J \varepsilon \quad (4a)$$

$$M = F_x R + J \varepsilon \approx F_n \mu R + J \varepsilon \quad (4b)$$

where  $F_x$ ,  $F_n$  are the components of the wheel–track force  $F$  along the  $x$ -axis, normal to the contact surface;  $R$  is the radius of the wheelset;  $J$  is the rotational inertia of the wheelset;  $\mu$  is the traction friction coefficient, taken as 0.03 [38];  $\varepsilon$

is the angular acceleration of the wheelset ( $\varepsilon = 0$ , due to the vehicle running at constant speed).

## 2.2 Modelling of corrugation

Rail corrugation is caused by rail surface wear. Different wavelengths are often associated. As a result, the excited wheel–rail vibration by corrugation also contains a variety of frequency components. However, on China high-speed railway lines, the operating vehicle type, operating speed, track type are identical. Consequently, the produced corrugation has a nearly fixed wavelength (Fig. 1) [6–8].

Therefore, in the wheel–rail dynamic model, corrugation was simulated by a cosine shaped rail surface, as shown in Fig. 4.

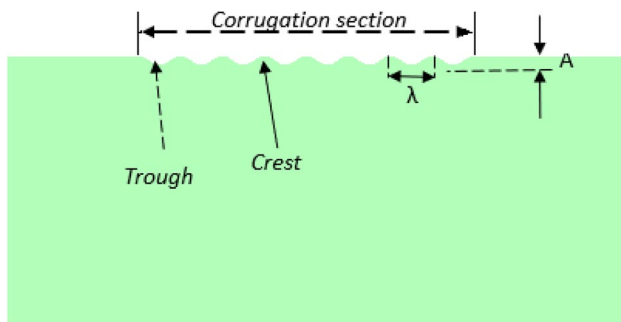


Fig. 4 Unevenness of the rail surface with corrugation

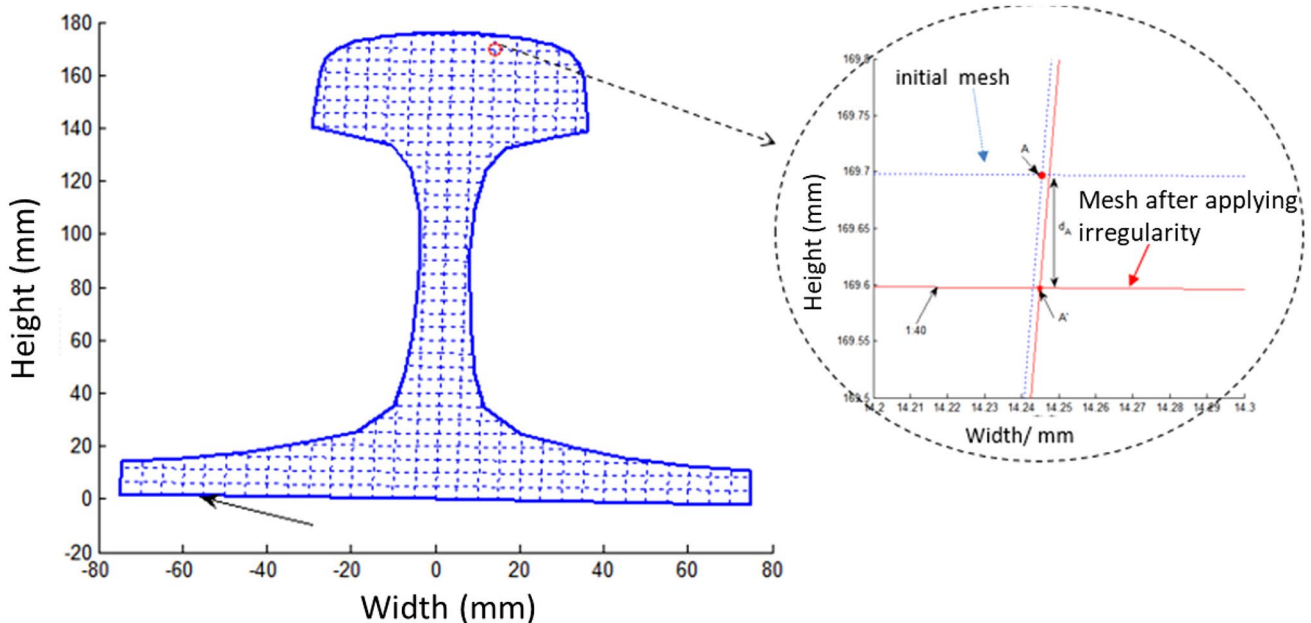


Fig. 5 Corrugation simulation means by modifying node coordination

Figure 4 shows that the rail wear  $\Delta$  periodically varies with the x-axis coordinate at any position in the corrugation section. The  $\Delta$  is calculated by Eq. 5.

$$\Delta(x, y, z) = \begin{cases} \frac{A}{2} \left( 1 - \cos\left(\frac{2\pi(x-x_a)}{\lambda}\right) \right) & x_b \geq x \geq x_a \\ 0 & x < x_a, x > x_b \end{cases} \quad (5)$$

where  $A$  is the corrugation depth value;  $\lambda$  is the corrugation wavelength;  $x_a$  and  $x_b$  are respectively the x-axis coordinates of the start point a and end point b of the corrugation section (Fig. 2). The wear at rail cross-section is corrected using the following correction formula:

$$\delta(x, y, z) = 1 - \left( \frac{y}{w_x} \right)^2 \quad |y| \leq w_x \quad (6)$$

where  $w_x$  is the width of the corrugation along the y-axis, i.e. half the width of the rail running surface.

In general, the width of the rail running surface ( $w_x$ ) is less than the width of the rail head ( $w$ ). In addition, the width of the rail running surface varies along the x-axis at the same period as the corrugation wavelength. The cosine function was used to simulate the variation of the width of the rail running surface along the y-axis in the corrugation section, as given by Eq. 7.  $w_1$  and  $w_2$  are the narrowest rail running surface and the half value of the widest rail running surface, respectively. Their values were taken as 15 mm and 20 mm, respectively, in the following models.

$$w_x = w_1 + \frac{w_2 - w_1}{2} \left( 1 - \cos\left(\frac{2\pi(x - x_a)}{\lambda}\right) \right) \quad x_b \geq x \geq x_a \quad (7)$$

The rail surface roughness is imposed by modifying the mesh node coordinates of the meshes in the corrugation section. As shown in Fig. 5, the correction amount of any grid node  $n_A(x_A, y_A, z_A)$  of the rail at Section  $ab$  is  $d_n$ , and the node coordinates  $n_{A'}(X_{A'}, Y_{A'}, Z_{A'})$  for simulating the corrugation are calculated using Eq. 8.

$$\begin{cases} d_n = \Delta_{(x_A, y_A, z_A)} * \delta_{(x_A, y_A, z_A)} \\ x_{A'} = x_A \\ y_{A'} = y_A + z_A \frac{d_n}{h} \cos(\theta) \\ z_{A'} = y_A - z_A \frac{d_n}{h} \sin(\theta) \end{cases} \quad x_a \leq x_A \leq x_b \quad (8)$$

where  $\theta$  is the 1:40 rail slope angle;  $h$  is the height of the rail (176 mm);  $d_n$  is calculated also according to the position of node  $n_A$ .

The rail roughness in corrugation section of the wheel–rail dynamics model was simulated using Eqs. 5, 6, 7, 8. It is a continuous cosine shape along the  $x$ -axis and a parabolic distribution along the  $y$ -axis. As shown in Fig. 6,

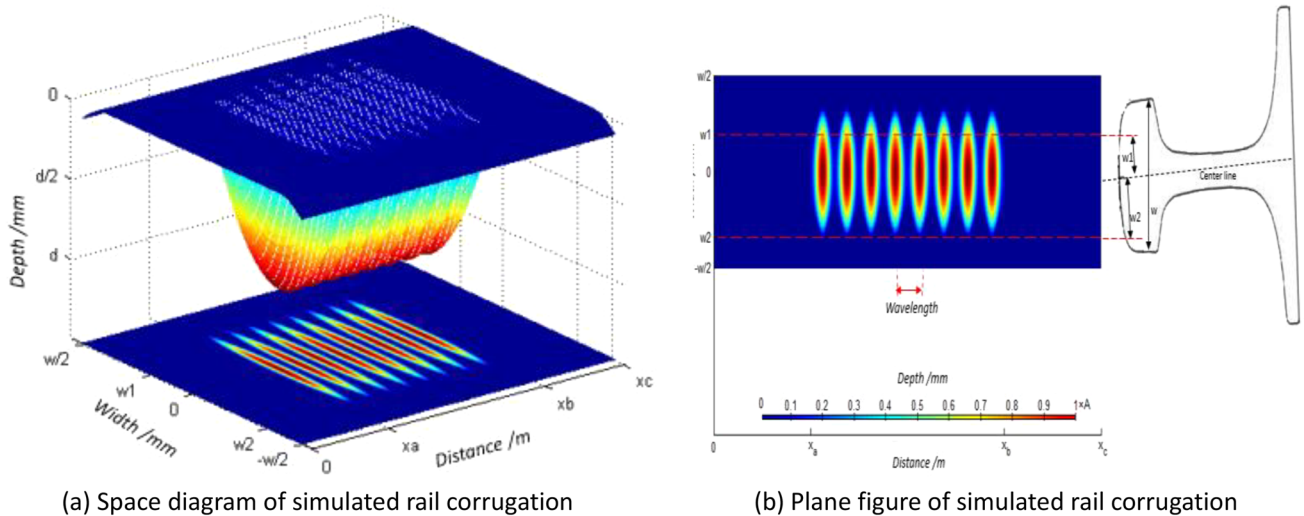
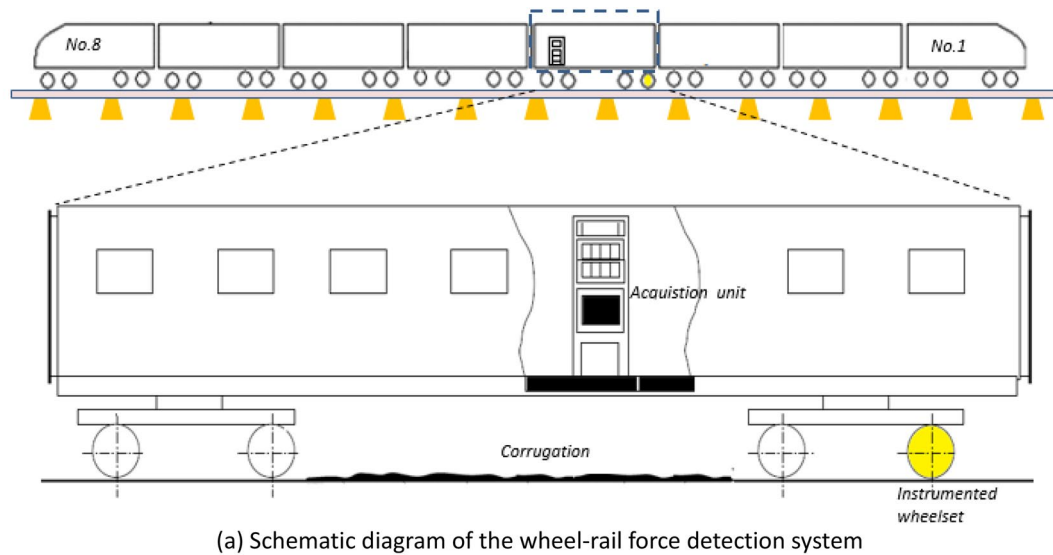


Fig. 6 Rail surface roughness demonstration after applying corrugation

Table 1 Parameters for wheel–track dynamics model

Parameters		Value	Unit	Parameters		Value	Unit
Wheel and rail materials	Poisson's ratio	0.3	–	Primary suspension (vertical)	Stiffness	1.04	kN/mm
	Density	7.8	mg/mm <sup>3</sup>		Damping	50.0	Ns/mm
	Modulus of elasticity	210.0	GPa	Primary suspension (lateral)	Stiffness	0.4	kN/mm
	Tangential modulus	21.0	GPa		Damping	60.0	Ns/mm
	Yield strength	800.0	MPa	Fastener support (vertical)	Stiffness	22.0	kN/mm
Track slab	Poisson's ratio	0.25	–		Damping	47.7	Ns/mm
	Density	2.4	mg/mm <sup>3</sup>	Mass per unit length of rail ( $m_r$ )		60.643	Kg/m
	Modulus of elasticity	34.5	GPa			14	10 <sup>3</sup> kg
Cement and asphalt mortar	Poisson's ratio	0.2	–	Track bed under CA mortar	Poisson's ratio	0.16	–
	Density	1.6	mg/mm <sup>3</sup>		Density	2.4	mg/mm <sup>3</sup>
	Modulus of elasticity	8.0	GPa		Modulus of elasticity	32.5	GPa
Static wheel weight ( $P_0$ )		70.3	kN	Sleeper spacing ( $L_r$ )		650.0	mm
Friction coefficient of wheel–rail		0.30	–	Wheelset shaft radius		30	mm
Wheel rolling radius		430	mm				



(b) Side view



(c) Front view

**Fig. 7** Wheel–rail force measurement system for high-speed trains

the darkness degree of the colour in the figure indicates the magnitude of corrugation depth value, and blue indicates the normal rail surface.

### 2.3 Model validation

The parameters for the wheel–rail dynamic model were determined according to in-service rolling stock, as shown in Table 1. The proposed model was first validated by comparing the simulated vertical forces with those measured in the field.

To measure the wheel–rail contact forces, a CRH3 high-speed comprehensive inspection train (developed by CARS) is equipped with a special wheelset. The schematic diagram of the wheel–rail force detection system is shown in Fig. 7. The special wheelset can measure high-frequency contact force between wheels and rails in real time [27, 29] with the frequency of output data at 4000 Hz. Particularly, the wheelset can be seen as a special sensor, using which WRVF in the field are measured.

The rail surface roughness was measured manually in the field, as shown in Fig. 8a. The sampling interval was set to

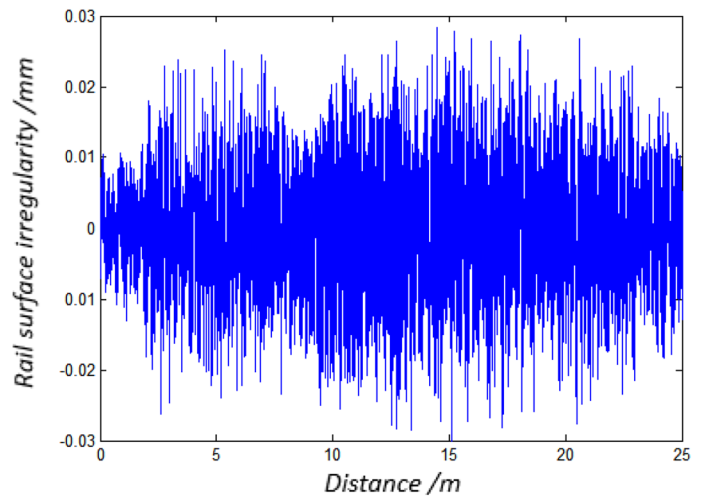
be 2 mm. Using 30–300 mm bandpass filter, the rail surface irregularity roughness lies between  $\pm 0.03$  mm, as shown in Fig. 8b. The spectrum has energy concentration characteristics, as shown in Fig. 8c, the maximum spectrum energy value corresponds to the spatial frequency of  $12.76 \text{ m}^{-1}$  and its multiples, such as  $25.51 \text{ m}^{-1}$ ,  $38.64 \text{ m}^{-1}$ ,  $51.03 \text{ m}^{-1}$ , etc. (with smaller spectrum energy). This indicates that the corrugation section has the main roughness with fixed wavelength. From the fundamental frequency, the main wavelength is calculated as approximately 78 mm.

The measured WRVF waveform and spectrum (using special wheelset) are shown in Fig. 9a. The WRVF fluctuates about the static wheel weight  $P_0$  and gradually increases with the increase of the corrugation depth. The fluctuation range is fixed at  $\pm 23$  kN at around 4.7 m. The WRVF spectrum has a local peak at 1083 Hz, as shown in Fig. 9b, which corresponds to the excitation of the main roughness with the fixed wavelength. Fig. 10 shows the comparison between the measured and calculated WRVFs. It is seen that they have the same trend and comparable amplitude in both time and frequency domains, as shown in the Figure 10 a and b. The time–frequency curve in Fig. 10 c and d show the

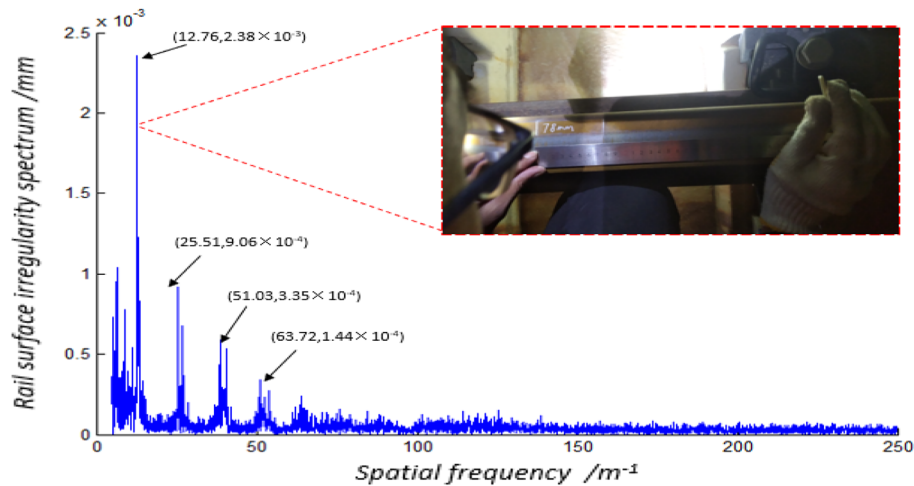




(a) Field measurement



(b) Rail surface irregularity



(c) Spectrum of rail surface roughness

**Fig. 8** Rail surface roughness measured in corrugation section

characteristics of the distribution of WRVF (with mileage and frequency using Fourier transform [39]). The measured vertical forces have three main frequency domains, i.e. 0, 125 and 1081 Hz. The frequency of 1081 Hz corresponds to the corrugation excitation frequency (roughness shown in Fig. 8b). The comparison shows that in the high-frequency domain, the measured results and simulation results are in good agreement. This indicates that the wheel–rail dynamics model is sufficiently accurate for the high-frequency response of the WRVF under corrugation excitation.

### 3 Numerical results and discussions

The corrugation on the high-speed railway lines in China has the wavelength in the range of 80–120 mm [40]. The corrugation depth is generally not greater than 0.4 mm. Therefore, the corrugation in the model was set to be in the range from 40 to 180 mm (increments at 5 mm), and the corrugation depth is from 0.02 mm to 1 mm. The WRVF under the train speed of 300 km/h for different corrugation wavelengths (40 mm, 100 mm and 180 mm) are shown in Fig. 11a–c. The minimum WRVF is 0 kN for special conditions in Fig. 11a and b, because the wheel–rail lose contact with each other.

The WRVF excited by the corrugation given in Fig. 11 periodically varies with the travel distance. The amplitude (around the static wheel weight  $P_0$ ) increases with the increase of the corrugation depth, as shown in Table 2,

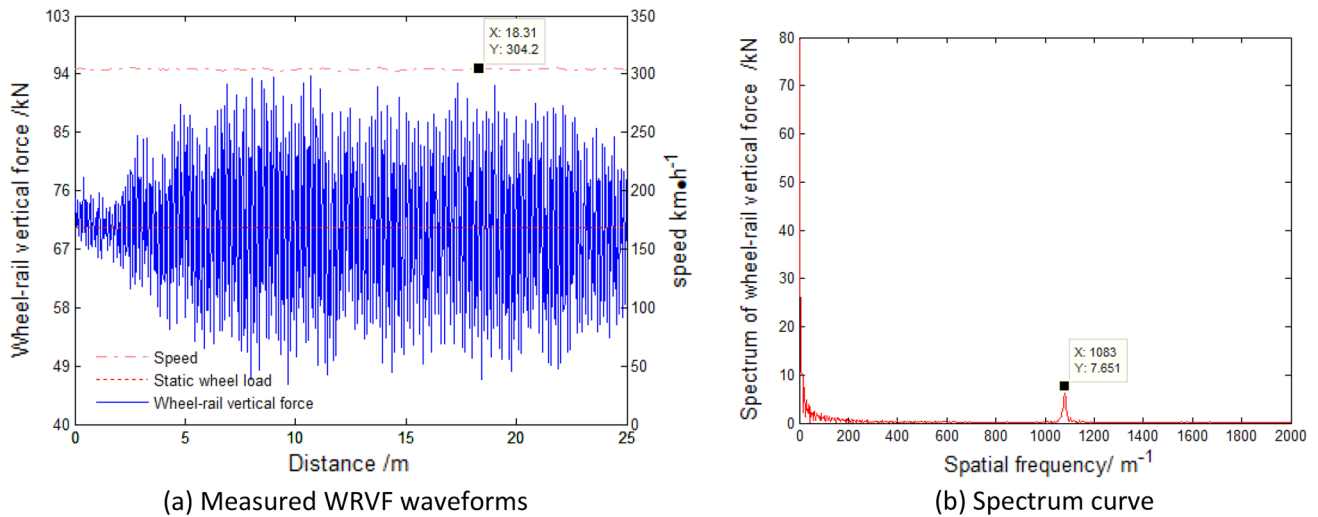


Fig. 9 Measured wheel-track vertical force in corrugation section

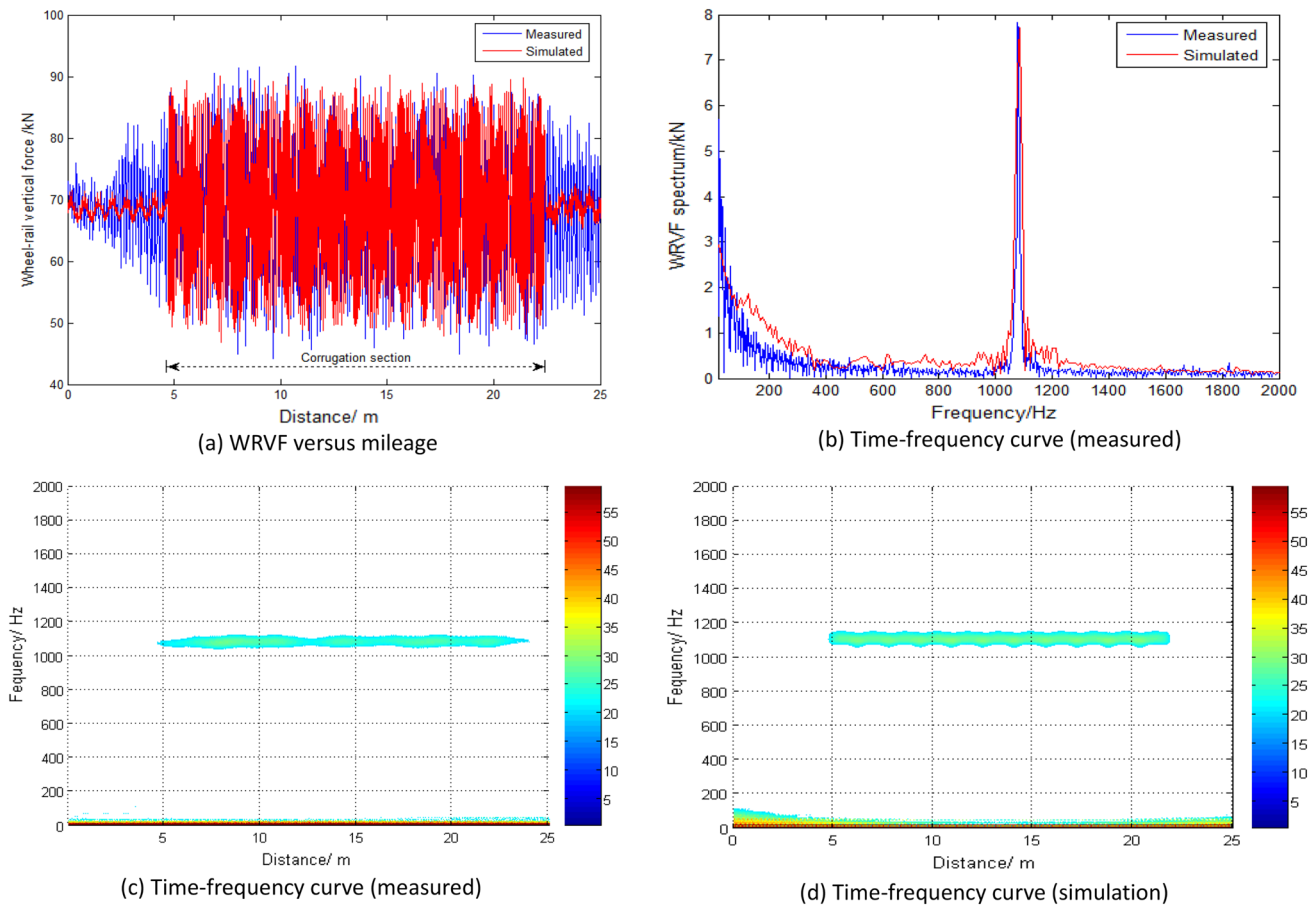
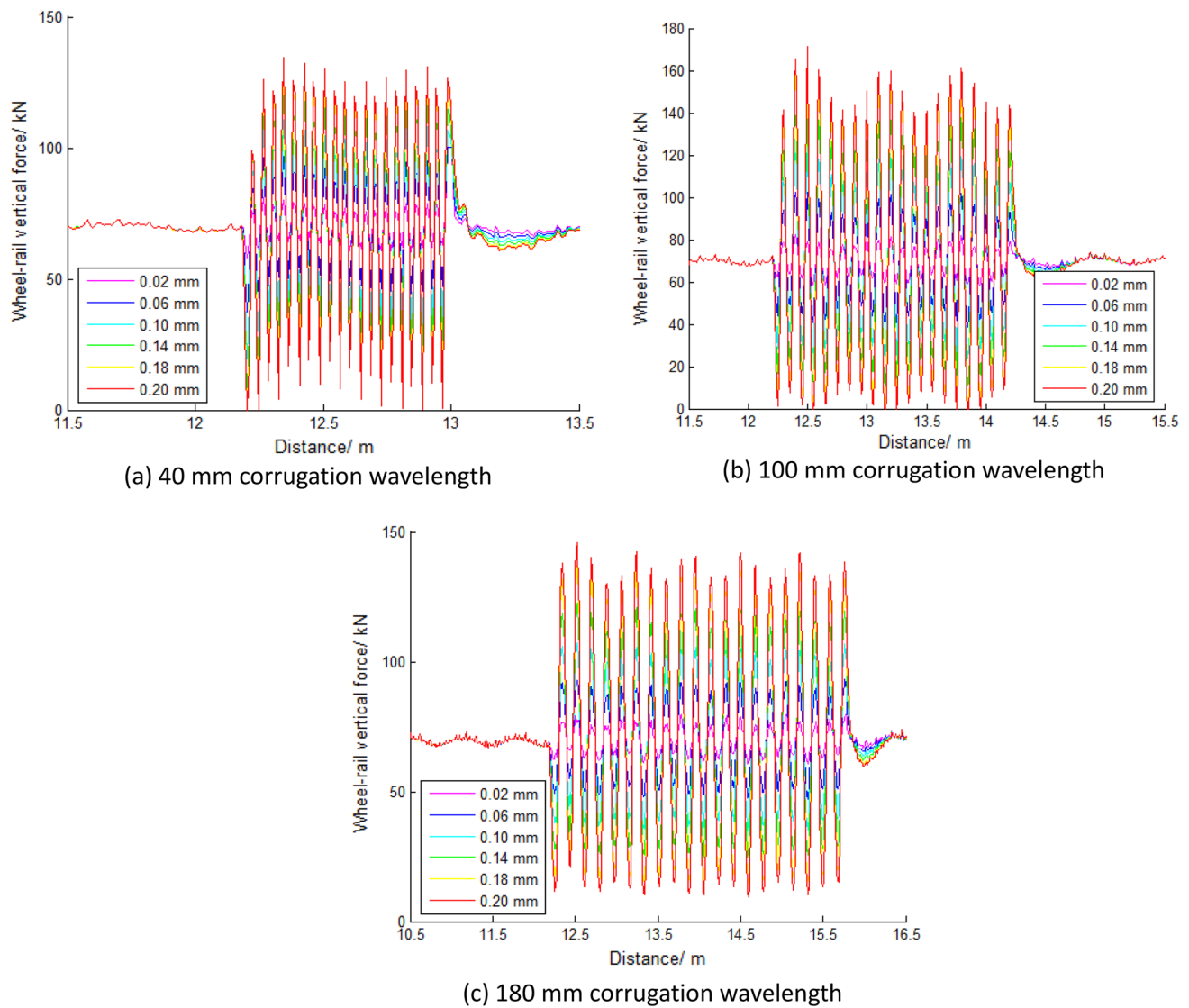


Fig. 10 Comparison of measured and simulated WRVF in time-frequency domain

which lists the amplitudes of the WRVF corresponding to different corrugation depths at the wavelength of 100 mm.

The WRVF (under the same corrugation depth) has non-linear relationship with corrugation wavelength. This can be observed from the relation between the minimum and



**Fig. 11** WRVF for three corrugation wavelengths

**Table 2** WRVF corresponding to different corrugation depths at the wavelength at 100 mm

Corrugation depth (mm)	0.02	0.06	0.10	0.14	0.18	0.20
WRVF (kN)	6.43	18.834	30.47	41.18	51.03	55.53

**Table 3** Wheel-track vertical force corresponds with different corrugation wavelength

Wavelength (mm)	40	100	140
Minimum value (kN)	0	0	13.34
Maximum value (kN)	125.4 kN	159.5	142.1

maximum values of the WRVF and the corresponding to the three sets of wavelengths under the corrugation depth of 0.2 mm, as given in Table 3.

Figure 11 also shows that the fluctuation range of WRVF for the corrugation wavelength of 100 mm is significantly larger than the results of other corrugation wavelengths. The waveform of the WRVF slightly varies due to a number of factors, such as discontinuous support of the sleepers and the position of the wheel-rail contact. The maximum value of the WRVF in one cycle cannot reflect the dynamic response of the wheel-rail interaction caused by corrugation. Therefore, the 3 standard deviation criteria ( $3\sigma$ ) of the maximum values of 10 cycles was used as the representative value of WRVF. The representative values of WRVF (different

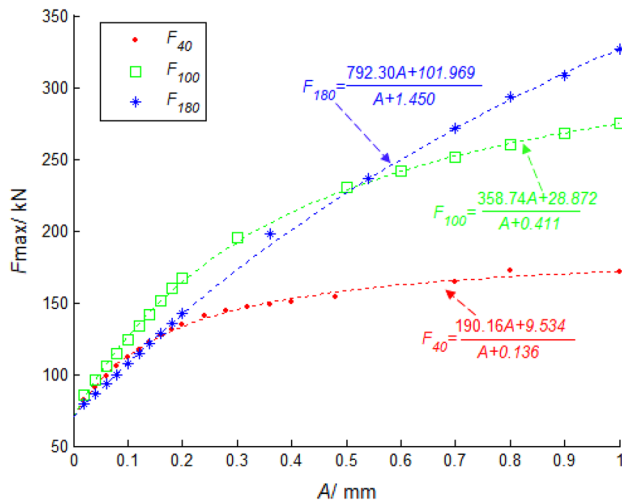


**Fig. 12** Wheel-track vertical force versus corrugation depth at different wavelengths

corrugation depths and wavelengths) are given in Fig. 12. The force of wavelength,  $\lambda$ , is noted as  $F_\lambda$ .

Figure 12 shows that the value of WRVF can be affected by both the wavelength and the depth. For example, when the depth is less than 0.18 mm, the WRVF ( $F_{40}$ ) is greater than  $F_{180}$  and less than  $F_{100}$ . When the depth is greater than 0.18 mm and less than 0.54 mm,  $F_{180}$  is less than  $F_{100}$  and greater than  $F_{40}$ . When the depth is greater than 0.54 mm,  $F_{100}$  is less than  $F_{180}$  and greater than  $F_{40}$ .

In addition, the correlations between the WRVF and depth have a similar trend for different wavelengths. The WRVF increases approximately linearly with the depth when the depth is relatively small. The increment of the WRVF slows down with the depth, when depth relatively is large.

This indicates that the rate of increase in the WRVF with the depth is dependent on the wavelength. This phenomenon is related to the contact position of wheel–rail interaction, as shown in Fig. 13, where the WRVF (wavelength 100 mm) and the wheel–rail contact positions can be observed.

Figure 13a shows that the minimum value of the WRVF is greater than 0 kN when the depth is less than 0.2 mm. This means the wheel–rail is not out of contact. The minimum value of WRVF is 0 kN when the depth is greater than 0.2 mm, which means the wheel–rail is out of contact at that time.

To be more specific, different colours are used to characterise the wheel–rail contact state in the wheel–rail dynamic model, as shown in Fig. 13b. The blue indicates the position of wheel–rail contact, while the grey indicates the position where the wheel–rail is out of contact. Figure 13b shows that when corrugation depth is less than 0.2 mm, the grid nodes on the rail surface roughness are all in blue, indicating that the wheel–rail is not out of contact under this condition. As the corrugation depth increases from 0.2 mm to 0.9 mm, the wheel–rail contact position is gradually concentrated near the corrugation peak. In addition, the wheel–rail contact position does not change much after the corrugation depth is greater than 0.5 mm. At this time, the WRVF waveform changes less with the increase of corrugation depth, which corresponds to the phenomenon shown in Fig. 12 (the WRVF was relatively little affected by corrugation depth).

The rational equation and the non-linear least squares method [41] were used to fit the relationship between the WRVF and the corrugation depth shown in Fig. 12. The following rational equation is used.

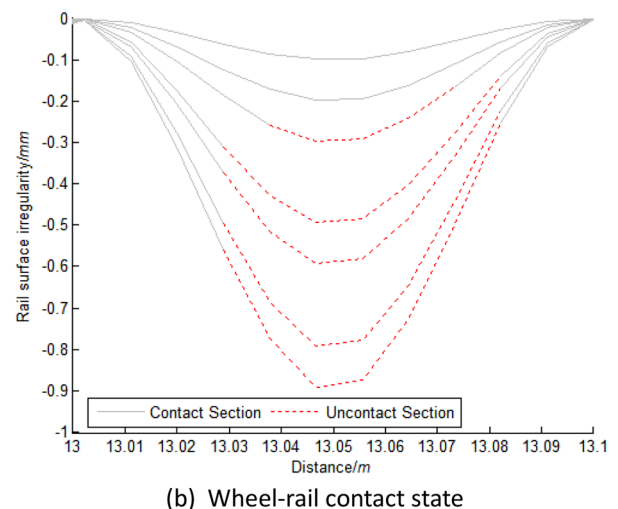
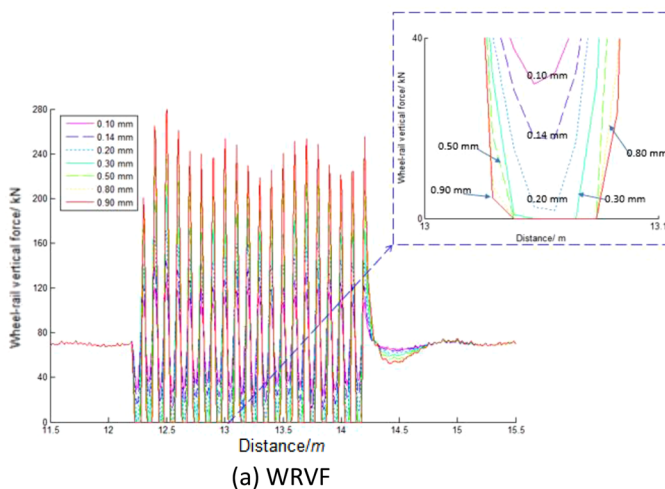


**Fig. 13** WRVF and wheel–rail contact position at 100 mm wavelength

**Table 4** Values for fitted curve parameters between WRVF and corrugation depth

Wavelength (mm)	$c_1$ (kN)	$c_2$ (kN)	$d_1$	Wavelength (mm)	$c_1$ (kN)	$c_2$ (kN)	$d_1$
40	190.16	9.534	0.136	112	466.24	49.410	0.703
44	198.34	10.560	0.150	116	486.19	53.257	0.758
48	213.48	9.833	0.140	120	516.26	46.072	0.656
52	231.26	11.397	0.162	124	547.69	63.663	0.906
56	247.65	17.044	0.242	128	507.14	57.738	0.821
60	281.49	17.359	0.247	132	479.73	54.892	0.781
64	291.72	20.706	0.295	136	474.99	54.696	0.778
68	271.85	19.288	0.274	140	454.06	49.836	0.709
72	265.65	17.691	0.252	144	472.66	56.729	0.807
76	270.6	15.764	0.224	148	478.18	53.918	0.767
80	275.31	17.594	0.250	152	534.69	69.070	0.983
84	307.18	20.057	0.285	156	545.05	61.297	0.872
88	312.87	19.109	0.272	160	589.44	75.179	1.070
92	347.68	28.753	0.409	164	672.34	91.505	1.302
96	354.75	27.808	0.396	168	697.12	93.316	1.328
100	358.74	28.872	0.411	172	717.96	93.608	1.332
104	377.34	31.327	0.446	176	739.86	98.454	1.401
108	423.57	38.621	0.550	180	792.30	101.969	1.450

$$F = \frac{c_1 A + c_2}{A + d_1} \quad (9)$$

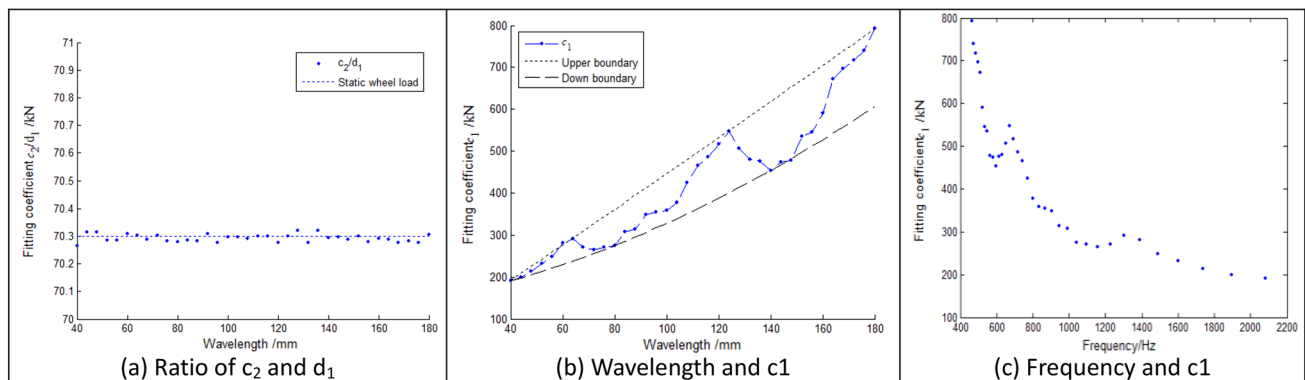
where  $c_1$ ,  $c_2$  and  $d_1$  are the parameters to be fitted.

Under the condition of that the fitness is over 0.995, the fitted curves between  $F_{40}$ ,  $F_{100}$ ,  $F_{180}$  and corrugation depth are obtained from Eq. 9, as shown in the dashed line in Fig. 12. The fitting coefficients are also given in the expressions. The mean squared error values of the three fitted curves are 0.89 kN, 1.70 kN and 1.59 kN, respectively. This means that the fitted curves between the WRVF and the corrugation depth have the same trend pattern as the scattered points. More importantly, the function fits well and has a small mean squared error value, indicating that

Eq. 9 can characterise the relationship between the WRVF and the corrugation depth.

Using the values of the fitted curve in Table 4, the relationship between the WRVF and corrugation depth is fitted by the rational equation (Eq. 9).

The parameters for fitting curve are reasonable, because they are in agreement with the inspection results. Specifically, the vertical wheel–rail force is small when the corrugation is slight. In other words, the WRVF at the 0 mm corrugation depth is close to the static wheel weight  $P_0$ . From Eq. 9, it can be seen that WRVF is then approximately equal to the ratio of the fitted parameters  $c_2$  and  $d_1$ . The scatter plot of the ratio of  $c_2$  to  $d_1$  with the different corrugation wavelengths (in Table 4) is shown in Fig. 14a. In addition, Eq. 9 shows that the value of  $F$  converges to

**Fig. 14** Scatterplot of fitted parameters as corrugation wavelength



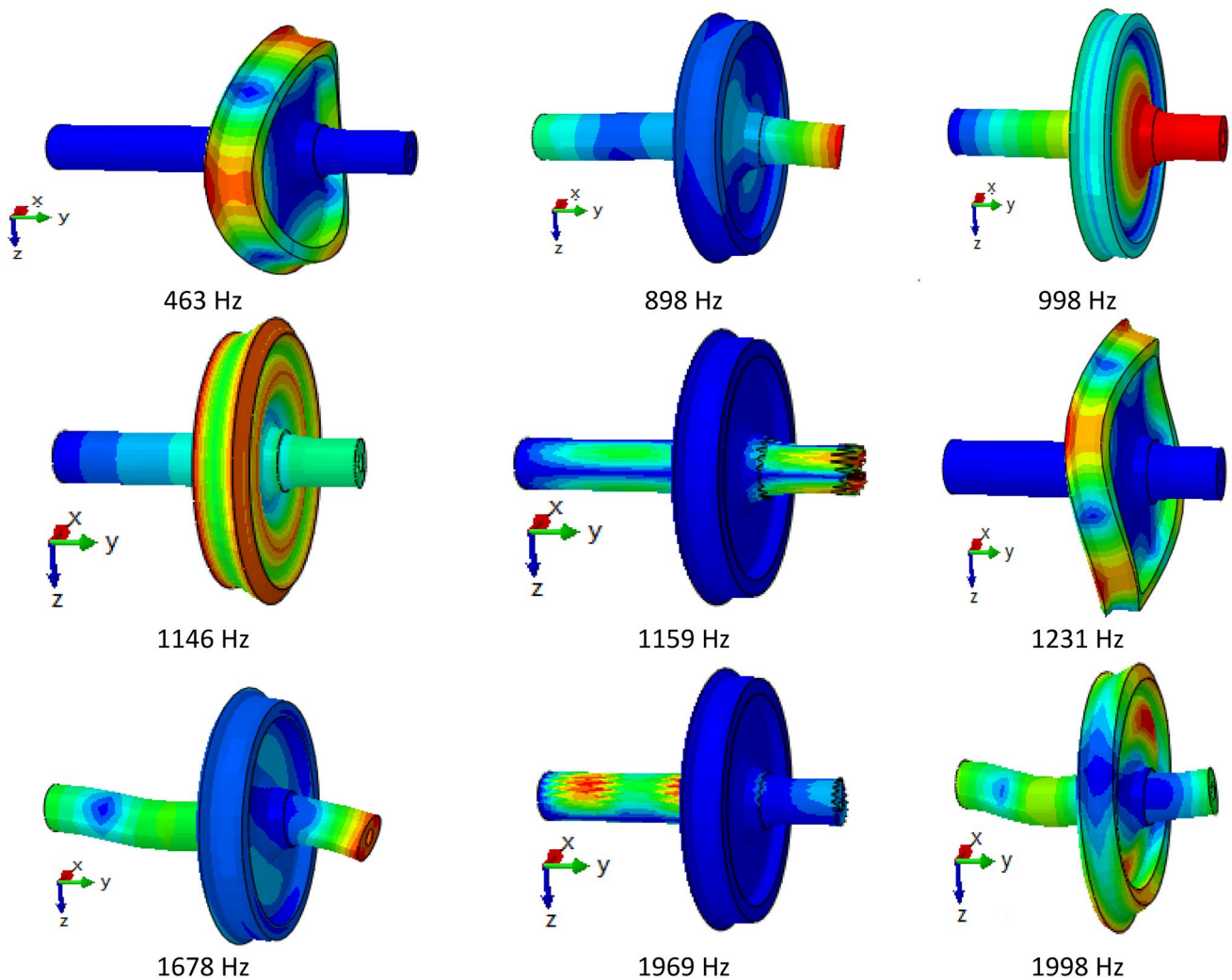


Fig. 15 Vibration modes for wheelset

the fitting parameter  $c_1$  when  $A$  is large, which can be reflected in Fig. 14b. Using Eq. 1, the correlation between  $c_1$  and frequency of wheel–rail excitation can be obtained, as shown in Fig. 14c.

The reasons for the unsmooth scatter of the fitted parameters ( $c_i$ ) with wavelength in Fig. 14b are discussed as follows.

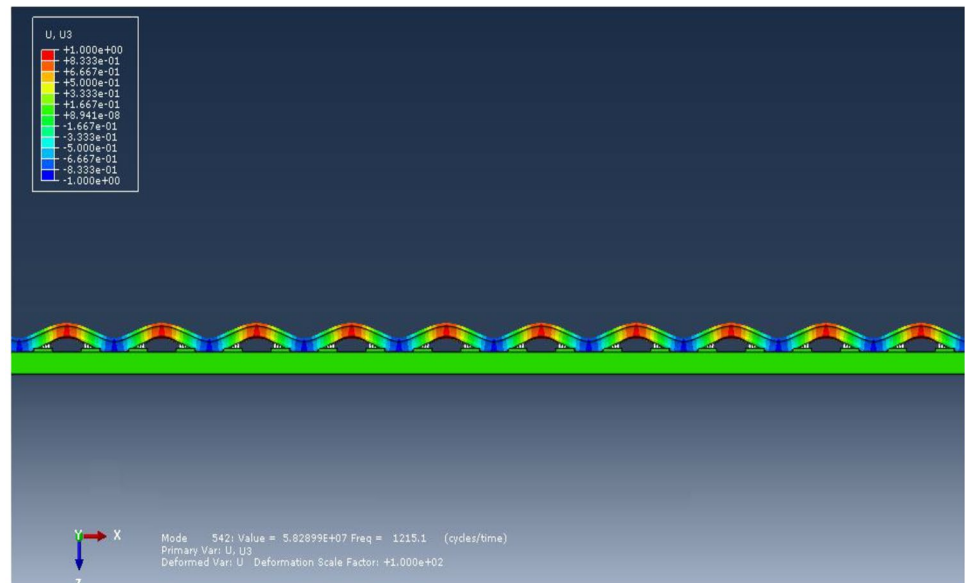
The frequency of wheel–rail excitation due to corrugation is related to the vehicle operating speed and the wavelength of the corrugation. The inherent vibration modes of the wheelset and rail are different under different excitation frequencies. From Eq. 1, the excitation frequencies of the 300 km/h with corrugation wavelengths of 40 to 180 mm are 463 to 2084 Hz. The vibration modes of wheelset are shown in Fig. 15.

The fitted parameter  $c_1$  increases with the increase in corrugation wavelength, fluctuating within the upper and lower boundaries. The local peaks in the curve are at wavelengths

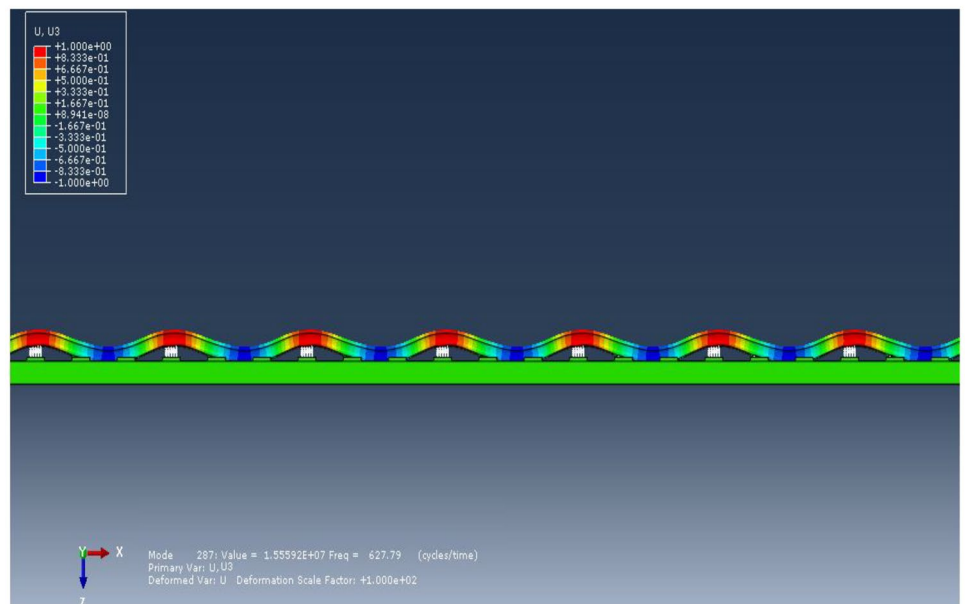
from 60 to 72 mm and 120 to 136 mm, as shown at positions A and B in Fig. 14b. The reason for the local peaks at positions A and B is related to the inherent vibration frequency of the rail. Position A corresponds to a frequency close to the rail Pinned–Pinned resonant frequency, when the rail vibration waveform standing wave node is located in the sleeper-supporting position. The wavelength is equal to 2 times of the sleeper spacing. The Pinned–Pinned resonant frequency ( $f_{pp}$ ) is calculated using Eq. 10 [42].

$$f_{pp} = n^2 \frac{\pi}{2L_r^2} \sqrt{\frac{EI}{m_r}} \quad (10)$$

where  $n$  is the Pinned–Pinned resonance frequency order.  $L_r$  is the rail sleeper spacing;  $m_r$  is the mass per unit length of rail.  $EI$  is the rail bending stiffness,  $6.62 \times 10^6$  N m<sup>2</sup>.

**Fig. 16** Rail vibration modes

(a) 1215.1 Hz



(b) 627.8 Hz

Using Eq. 10 and model parameters in Table 1, when  $n=1$  the 1st order rail Pinned–Pinned resonance frequency is approximately 1227.8 Hz. Its half frequency is 614 Hz, which corresponds to a rail vibration wavelength, approximately 3 times the sleeper spacing. The numerical simulation results of the Pinned–Pinned resonant frequency of the rail is approximately 1215.1 Hz, which is close to the result calculated by Eq. 10, as shown in Fig. 16.

Under the conditions (300 km/h train speed, 60–72 and 120–136 mm corrugation wavelengths), the wheel–rail vibration frequencies are 1157.4–1388.9 Hz and 612.7–694.4 Hz, respectively. The frequency bands are close to the rail Pinned–Pinned resonance frequency and its half value,

respectively. The wheel and rail resonates near this frequency band at wheel–rail contacts, for which the wheel–rail interaction is improved. As the WRVF increase, the fitting coefficient  $c_1$  is increased as well. The modal vibration patterns of the rail model 1215.1 Hz and its half frequency of 627.8 Hz are shown in Fig. 16.

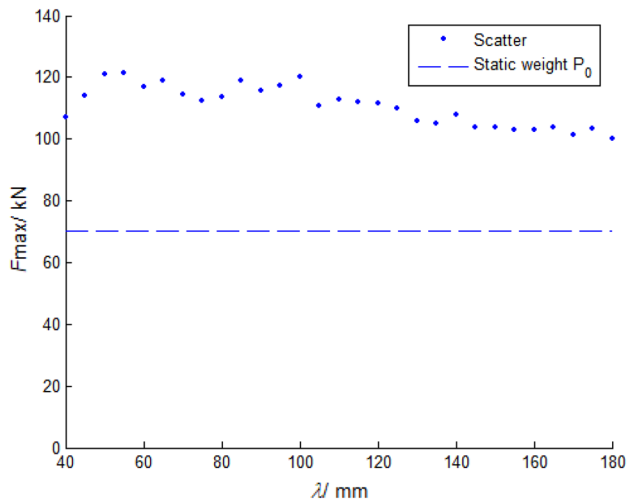


Fig. 17 WRVF vs. wavelength for 0.08 mm corrugation depth

## 4 Indicator for rail grinding

### 4.1 Indicator calculation method

The corrugation depth value of 0.08 mm [18] is used as a reference for rail grinding in the maintenance regulations of China. The scatter diagram of the WRVF under the condition of different wavelengths and depth values of 0.08 mm is shown in Fig. 17.

Figure 17 shows that at wavelengths of 40 to 180 mm, the WRVF under 0.08 mm corrugation depth ranges from 100.18 to 121.48 kN, whose difference (21.3 kN) is about 30.31% of the static wheel weight  $P_0$ . Therefore, it is not sufficient to only use the WRVF from the wheel–rail force detection system (Fig. 7) to make grinding decisions. The influence of corrugation wavelength should be considered.

When the corrugation depth is less than 0.2 mm, the wheel–rail is not detached from each other for a long time. The WRVF  $F$  can be written as the sum of the static wheel weight  $P_0$  and the maximum value of the wheel–rail vertical additional force  $P_{\text{dny}}$  [43].

$$F = P_0 + P_{\text{dny}} \quad (11)$$

The ratio of the fitted parameters  $c_2$  to  $d_1$  is approximately equal to the static wheel weight  $P_0$ , by which the Eq. 9 can be written as Eq. 12.

$$F = \frac{(c_1 - \frac{c_2}{d_1})A}{A + d_1} + \frac{c_2}{d_1} \approx \frac{(c_1 - P_0)A}{A + d_1} + P_0 \quad (12)$$

From Eq. 11 and Eq. 12, the wheel–rail vertical additional force  $P_{\text{dny}}$  can be calculated, as shown in Eq. 13.

$$P_{\text{dny}} \approx \frac{(c_1 - P_0)A}{A + d_1} \quad (13)$$

Excessive wheel–rail vertical additional forces can cause fatigue damages to the track structure [44]. Therefore, based on wheel–rail vertical additional force, the indicator normalised to the corrugation wavelength is calculated as follows.

$$I_A = \frac{P_{\text{dny},\lambda}}{P_{\text{dny},\lambda,A}} \quad (14)$$

In Eq. 14,  $I_A$  is the indicator value when the corrugation depth limit for grinding is  $A$ . When  $I_A$  is greater than or equal to 1, grinding should be taken;  $A$  is normally taken as 0.08 mm;  $P_{\text{dny},\lambda}$  is the wheel–rail vertical additional force that is obtained by special wheelset measurement. It has the corrugation wavelength as  $\lambda$ ;  $P_{\text{dny},\lambda,A}$  is wheel–rail vertical additional force obtained by Eq. 13. It has the wavelength  $\lambda$  and depth  $A$  of corrugation, which corresponds to the value in Table 4.

The parameters  $c_1$  and  $d_1$  in Eq. 13 are related to the corrugation wavelength ( $\lambda$ ), and  $\lambda$  can be obtained from the corrugation excitation frequency and train speed (Eq. 1). Therefore, when calculating the value of  $I_A$ , the WRVF data are first converted to a frequency domain signal by time–frequency conversion techniques, such as the Fourier transform [44] or Hilbert–Yellow transform [39]. The main frequency of energy spectrum in the WRVF frequency domain signal determines the excitation frequency of the corrugation.

When there are multiple wavelengths of corrugation, the wavelengths are arranged in order of the spectrum magnitude of the wheel–rail vertical droop force. The wavelengths are defined as  $\lambda_1, \lambda_2, \dots$ . In this case, the grinding maintenance indicator value is the sum of the  $I_{A,i}$  corresponding to each wavelength, as shown in Eq. 15.

$$I = \sum_{i=1}^m I_{A,i} \quad (15)$$

In Eq. 15,  $i$  is the number of corrugation wavelengths involved in the calculation (1, 2, ...,  $m$ );  $I_{A,i}$  is the  $i$ -th wavelength component corresponding to the grinding indicator value.

### 4.2 Indicator validation

Field measurement was performed to validate the indicator for grinding. Specifically, based on the special wheelset measurement data and numerical simulation results (wheel–rail vertical additional forces), the location that needs grinding was found (predicted by the indicator). Afterwards, the field measurement of the rail corrugation at

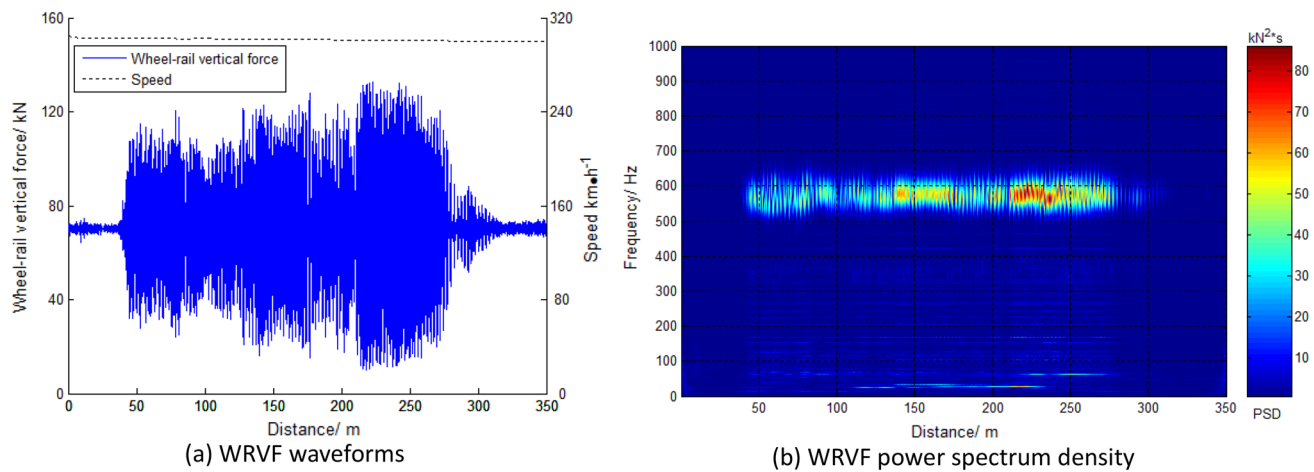


Fig. 18 WRVF waveforms and power spectrum density



Fig. 19 Corrugation observation of measured corrugation section

the location was performed to check that the rail condition. Details are explained as follows.

Figure 18 shows the waveform and the corresponding time–frequency curve of the WRVF, which were measured by a high-speed comprehensive inspection train (developed by CARS) passing through a corrugation section (approximately 285 m length). From Fig. 18a, it can be seen that the WRVF in the 35–350 m section are significantly greater than in the other sections. Figure 18b shows the WRVF at 582 Hz has a concentration.

Based on Eq. 1 and the train speed (302 km/h), the main wavelength of this corrugation is approximately 144 mm. The measured  $P_{\text{dny}}$  in the corrugation section is about 57.13 kN. Using Eq. 13 and the parameters in Table 4, the wheel–rail vertical additional force  $P_{\text{dny},144,0.08}$  is 36.29 kN.

Using Eq. 15, the indicator for grinding  $I_{0.08}$  is calculated as  $1.57 > 1$ , indicating that the corrugation at this section should be performed with rail grinding.

Figure 8a present the field measurement that was performed for the corrugation measurement. The corrugation wavelength is about 144 mm and maximum corrugation depth is about 0.15 mm (Fig. 19), which means this corrugation section has reached the limit of rail grinding. This is consistent with the judgement made by the indicator for grinding.

To further develop and validate the indicator for grinding, 40 corrugation sections were compared, by which the reliability of the indicator for grinding was obtained.

Specifically, using the high-speed comprehensive inspection train, the WRVF of 40 sections were identified with high value of indicator for grinding. This means the 40 sections need rail grinding according to the developed indicator. The consistency between the indicator value and the grinding operation was evaluated using method in [45], as shown in Fig. 20a. The diagram is divided into 4 zones depending on whether the I-value is greater than 1 and whether the grinding operation should be carried out. The respective definitions are as follows:

- Upper right quadrant I, “true positive” zone: the index value  $I \geq 1$ , and the corrugation is so severe that the grinding operation must be performed.
- Upper left quadrant II, “false positive” zone: the index value  $I \geq 1$ , but the real state of the corrugation doesn’t reach the maintenance limit. Grinding didn’t need to carry out.
- Lower left quadrant III, “true negative” zone: the index value  $I < 1$ , The corrugation is not severe enough to be grinded.

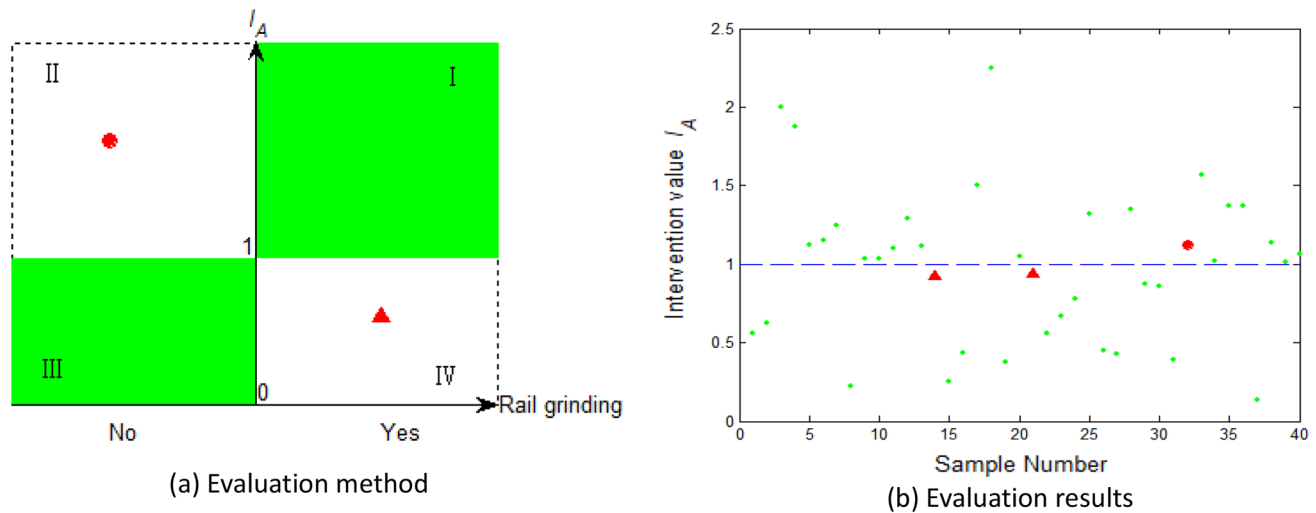


Fig. 20 Evaluation method and evaluation results of grinding indicator value  $I$

- Lower right quadrant IV, “false negative” zone: the index value  $I < 1$ , but the corrugation must be grinded.

From the above definitions, it can be seen that the upper right and lower left regions indicate that the grinding decisions based on the indicator value are correct (green areas in quadrant I and quadrant III in Fig. 20). The corresponding evaluated samples are shown in green. The other two areas indicate that the decisions are not correct, and the corresponding evaluated samples are shown in red solid circles and upper triangles. 40 indicator values are distributed between 0.22 and 2.25, and the indicator values are shown in Fig. 20b.

Figure 20b shows only one “false positive” sample was found, which indicates that the indicator has a low misjudgement rate when used for grinding decisions. In addition, the indicator value has the correct prediction 37 of 40 times, making the accuracy of the indicator approximately 92.5%. In addition, two “false negative” can be avoided by reducing the indicator limitation value from 1 to 0.9, by which the number of “false negative” samples can be effectively removed. Then, the accuracy can be improved to 97.5%.

## 5 Conclusions

To propose an accurate indicator for rail grinding (corrugation treatment), a wheel–rail dynamic model was developed with consideration of the vehicle and track parameters of typical high-speed railway lines in China. The numerical model was validated using the measured WRVF by the special wheelset developed by CARS. The indicator was calculated as the ratio of the measured WRVF and the calculated

WRVF by the proposed FE model. The conclusions are given as follows.

It is not sufficient accurate if only the WRVF is used as the indicator for the rail grinding decision. Because the correlation between the WRVF and the corrugation depth is influenced by the corrugation wavelength. At a fixed wavelength, the WRVF nonlinearly increases with the increase of the corrugation depth, and then gradually approaches a fixed value.

At the train speed of 300 km/h, the wheel–rail interaction response frequencies excited by corrugation with wavelengths at 60–72 mm and 120–136 mm are close to the rail Pinned–Pinned resonance frequency and its half value, respectively.

The proposed indicator for rail grinding decision can be used for the high-speed railway line (300 km/h) with the accuracy of 92.5%. As the wheel–rail force data are affected by track geometry irregularities, wheel–rail matching, vehicle vibration characteristics and equipment accuracy, it is recommended that the indicator limit is taken as 0.9. This can reduce the misjudgement possibility.

High-speed railway lines in China have various types of track structures and operating vehicles. The simulated track and vehicle are relatively simple. The proposed indicator is validated to be effective for monitoring corrugation on high-speed railway lines. Future works should propose a universal indicator based on the WRVF for the assessment of the corrugation states on all types of track and vehicles. In this case, more scientific supports for rail grinding decisions can be provided.

**Acknowledgements** This research is funded by the Key Research and Development Project of the China Academy of Railway Sciences Corporation Limited (2021YJ256 and 2021YJ022).



**Data availability** The authors confirm that the data supporting the findings of this study are available within the article [and/or] its supplementary materials.

**Open Access** This article is licensed under a Creative Commons Attribution 4.0 International License, which permits use, sharing, adaptation, distribution and reproduction in any medium or format, as long as you give appropriate credit to the original author(s) and the source, provide a link to the Creative Commons licence, and indicate if changes were made. The images or other third party material in this article are included in the article's Creative Commons licence, unless indicated otherwise in a credit line to the material. If material is not included in the article's Creative Commons licence and your intended use is not permitted by statutory regulation or exceeds the permitted use, you will need to obtain permission directly from the copyright holder. To view a copy of this licence, visit <http://creativecommons.org/licenses/by/4.0/>.

## References

1. S. Kaewunruen, (2018) Monitoring of rail corrugation growth on sharp curves for track maintenance prioritisation. *The International Journal of Acoustics And Vibration* 23 (1).
2. Zhao X, Zhang P, Wen Z (2019) On the coupling of the vertical, lateral and longitudinal wheel–rail interactions at high frequencies and the resulting irregular wear. *Wear* 430–431:317–326
3. Y. Ye, B. Zhu, P. Huang, B. Peng, (2022) OORNet: A deep learning model for on-board condition monitoring and fault diagnosis of out-of-round wheels of high-speed trains, *Measurement*.
4. Xu L, Zhai W, Chen Z (2018) On use of characteristic wavelengths of track irregularities to predict track portions with deteriorated wheel/rail forces. *Mech Syst Signal Process* 104:264–278
5. S. Li, Z. Li, A. Núñez, R. Dollevoet, (2017) New Insights into the Short Pitch Corrugation Enigma Based on 3D-FE Coupled Dynamic Vehicle-Track Modeling of Frictional Rolling Contact, *Applied Sciences* 7 (8)
6. Grassie SL (2009) Rail corrugation: Characteristics, causes, and treatments range. *Proceed Inst Mechan Eng, Part F: J Rail Rapid Transit* 223(6):581–596
7. Grassie S, Kalousek J (1993) Rail corrugation: characteristics, causes and treatments range. *Proceed Inst Mechan Eng, Part F: J Rail Rapid Transit* 207(1):57–68
8. Grassie SL (2005) Rail corrugation: advances in measurement, understanding and treatment. *Wear* 258(7–8):1224–1234
9. Sato Y, Matsumoto A, Knothe K (2002) Review on rail corrugation studies. *Wear* 253(1–2):130–139
10. Matsumoto A, Sato Y, Ono H, Tanimoto M, Oka Y, Miyauchi E (2002) Formation mechanism and countermeasures of rail corrugation on curved track. *Wear* 253(1–2):178–184
11. M. Hiensch, J.C. Nielsen, E.J.W. Verheijen, (2002) Rail corrugation in The Netherlands—measurements and simulations, 253(1–2) 140–149.
12. P.T. Torstensson, J.C.O. Nielsen, Rail Corrugation Growth on Curves – Measurements, Modelling and Mitigation, *Noise and Vibration Mitigation for Rail Transportation Systems* 2015, pp. 659–666.
13. Torstensson PT, Nielsen JCO (2009) Monitoring of rail corrugation growth due to irregular wear on a railway metro curve. *Wear* 267(1–4):556–561
14. Wu TX (2011) Effects on short pitch rail corrugation growth of a rail vibration absorber/damper. *Wear* 271(1–2):339–348
15. Du X, Jin X, Zhao G, Wen Z, Li W, Mazilu T (2021) Rail Corrugation of High-Speed Railway Induced by Rail Grinding. *Shock Vib* 2021:1–14
16. Liang H, Li W, Zhou Z, Wen Z, Li S, An D (2021) Investigation on rail corrugation grinding criterion based on coupled vehicle–track dynamics and rolling contact fatigue model. *J Vib Control* 28(9–10):1176–1186
17. W. Zhai, X. Jin, Z. Wen, X. Zhao, (2020) Wear Problems of High-Speed Wheel/Rail Systems: Observations, Causes, and Countermeasures in China, *Applied Mechanics Reviews* 72 (6).
18. I.O.f.S.J.S.N. (2013), *Acoustics–Railway applications–Measurement of noise emitted by railbound vehicles*.
19. M.o.R.o.t.p.s.R.o. 2013 China, *Maintenance Rules for Ballastless Track of High Speed Railway (Trial)*, TG/GW 115 2012, China Railway Publishing House, Beijing.
20. W. Zhao, W. Qiang, F. Yang, G. Jing, Y. Guo, Ballast layer defect inspection using data analysis of track irregularity.
21. Gazafrudi SMM, Younesian D, Torabi M (2021) A High Accuracy and High Speed Imaging and Measurement System for Rail Corrugation Inspection. *IEEE Trans Industr Electron* 68(9):8894–8903
22. H.-M. Thomas, T. Heckel, G.J.I.-N.-D.T. Hanspach, C. Monitoring, (2007) Advantage of a combined ultrasonic and eddy current examination for railway inspection trains, 49 (6) 341–344.
23. Haigermoser A, Lubert B, Rauh J, Gräfe G (2015) Road and track irregularities: measurement, assessment and simulation. *Veh Syst Dyn* 53(7):878–957
24. Boccione M, Caprioli A, Cigada A, Collina A (2007) A measurement system for quick rail inspection and effective track maintenance strategy. *Mech Syst Signal Process* 21(3):1242–1254
25. Salvador P, Naranjo V, Insa R, Teixeira P (2016) Axlebox accelerations: Their acquisition and time–frequency characterisation for railway track monitoring purposes. *Measurement* 82:301–312
26. Bagheri VR, Younesian D, Tehrani PH (2018) A new methodology for the estimation of wheel–rail contact forces at a high-frequency range. *Proceed Inst Mechan Eng, Part F: J Rail Rapid Transit* 232(10):2353–2370
27. Maglio M, Vernersson T, Nielsen JCO, Pieringer A, Söderström P, Regazzi D, Cervello S (2021) Railway wheel tread damage and axle bending stress – Instrumented wheelset measurements and numerical simulations. *International Journal of Rail Transportation* 10(3):275–297
28. Nielsen JCO (2008) High-frequency vertical wheel–rail contact forces—Validation of a prediction model by field testing. *Wear* 265(9–10):1465–1471
29. Nielsen JC (2008) Rail roughness level assessment based on high-frequency wheel–rail contact force measurements. *Springer, Noise and vibration mitigation for rail transportation systems*, pp 355–362
30. Gullers P, Andersson L, Lundén R (2008) High-frequency vertical wheel–rail contact forces—Field measurements and influence of track irregularities. *Wear* 265(9–10):1472–1478
31. Afferrante L, Ciavarella M (2009) Short-pitch rail corrugation: a possible resonance-free regime as a step forward to explain the “enigma”? *Wear* 266(9–10):934–944
32. Wei L, Quan-jun Z, Shi-you Z, Jia-feng F, Xue-song J (2015) Effect of metro rail corrugation on dynamic behaviors of vehicle and track. *J Traffic Transport Eng* 15(1):34–42
33. Kouroussis G, Caucheteur C, Kinet D, Alexandrou G, Verlinden O, Moeyaert V (2015) Review of trackside monitoring solutions: from strain gages to optical fibre sensors. *Sensors (Basel)* 15(8):20115–20139
34. Torstensson PT, Nielsen JC, Baeza L (2012) High-Frequency Vertical Wheel–Rail Contact Forces at High Vehicle Speeds-The Influence of Wheel Rotation. *Springer, Noise and Vibration Mitigation for Rail Transportation Systems*, pp 43–50

35. T. Belytschko, W.K. Liu, B. Moran, K. Elkhodary, *Nonlinear finite elements for continua and structures*, John Wiley and sons 2014.
36. Alarcón GI, Burgelman N, Meza JM, Toro A, Li Z (2016) Power dissipation modeling in wheel/rail contact: Effect of friction coefficient and profile quality. *Wear* 366–367:217–224
37. C. Esvelde, C. Esvelde, *Modern railway track*, MRT-productions Zaltbommel, The Netherlands 2001.
38. Baek K-S, Kyogoku K, Nakahara T (2008) An experimental study of transient traction characteristics between rail and wheel under low slip and low speed conditions. *Wear* 265(9–10):1417–1424
39. Tsai H-C, Wang C-Y, Huang NE, Kuo T-W, Chieng W-H (2014) Railway track inspection based on the vibration response to a scheduled train and the Hilbert-Huang transform range. *Proceed Inst Mechan Eng, Part F: J Rail Rapid Transit* 229(7):815–829
40. Li G, Zhang Z, Zu HJCRS (2019) Experimental study on wheel–rail force response characteristics under typical track defects of high speed railway 40(6):30–36
41. Al-Baali M, Fletcher R (1985) Variational methods for non-linear least-squares. *Journal of the Operational Research Society* 36(5):405–421
42. De Man AP (2002) A survey of dynamic railway track properties and their quality. Delft University of Technology, TU Delft
43. Fang G, Wang Y, Peng Z, Wu T (2018) Theoretical investigation into the formation mechanism and mitigation measures of short pitch rail corrugation in resilient tracks of metros. *Proceed Inst Mechan Eng, Part F: J Rail Rapid Transit* 232(9):2260–2271
44. Steenbergen MJMM, Esvelde C (2006) Relation between the geometry of rail welds and the dynamic wheel - rail response: Numerical simulations for measured welds. *Proceed Inst Mechan Eng, Part F: J Rail Rapid Transit* 220(4):409–423
45. C. Schwenke, A. (2014) Schering, True positives, true negatives, false positives, false negatives, Wiley StatsRef: Statistics Reference Online.

**Publisher's Note** Springer Nature remains neutral with regard to jurisdictional claims in published maps and institutional affiliations.